Available online at www.sciencedirect.com

ScienceDirect

Acta Materialia 80 (2014) 392–399

Acta MATERIALIA

www.elsevier.com/locate/actamat

Deformation-induced phase transformation in 4H–SiC nanopillars

Bin Chen [a], Jun Wang [b,c], Yiwei Zhu [a], Xiaozhou Liao [a,*], Chunsheng Lu [d], Yiu-Wing Mai [a], Simon P. Ringer [a,e], Fujiu Ke [f], Yaogen Shen [c]

[a] School of Aerospace, Mechanical and Mechatronic Engineering, The University of Sydney, Sydney, NSW 2006, Australia
[b] State Key Laboratory of Nonlinear Mechanics, Institute of Mechanics, Chinese Academy of Sciences, Beijing 100190, China
[c] Department of Mechanical and Biomedical Engineering, City University of Hong Kong, Kowloon, Hong Kong, China
[d] Department of Mechanical Engineering, Curtin University, Perth, WA 6845, Australia
[e] Australian Centre of Microscopy and Microanalysis, The University of Sydney, Sydney, NSW 2006, Australia
[f] School of Physics and Nuclear Energy Engineering, Beihang University, Beijing 100191, China

Received 21 July 2014; accepted 27 July 2014
Available online 3 September 2014

Abstract

The deformation behaviour of single-crystal SiC nanopillars was studied by a combination of in situ deformation transmission electron microscopy and molecular dynamics simulations. An unexpected deformation-induced phase transformation from the 4H hexagonal structure to the 3C face-centred cubic structure was observed in these nanopillars at room temperature. Atomistic simulations revealed that the 4H to 3C phase transformation follows a stick–slip process with initiation and end stresses of 12.1–14.0 and 7.9–9.0 GPa, respectively. The experimentally measured stress of 9–10 GPa for the phase transformation falls within the range of these theoretical upper and lower stresses. The reasons for the phase transformation are discussed. The finding sheds light on the understanding of phase transformation in polytypic materials at low temperature.

Keywords: SiC nanopillars; Phase transformation; In situ deformation; Transmission electron microscopy; Molecular dynamics

1. Introduction

Polymorphism is a phenomenon in which a compound exists in more than one crystalline structure. When the crystalline structures have the same atomic plane, which is usually a close-packed plane, and differ only in stacking sequence along the direction normal to the plane, this one-dimensional polymorphism is called polytypism. Polytypism commonly occurs in II–VI, III–V and IV–IV compound materials [1,2]. Silicon carbide (SiC) is a particularly important and interesting material since it has over 200 crystalline polytypic structures with common structural units of face-centred cubic zinc blende (ZB), hexagonal close-packed wurtzite (WZ) and rhombohedral structures [1]. Among these polytypes, the 4H–SiC structure with a bandgap of ~3.2 eV possesses favourable electrical properties, including high electron mobility [3,4], making SiC an attractive candidate for "green energy" components in high-power electronic applications because of the potential for saving electric power and reducing CO_2 emission [5–10]. The mechanical behaviour of semiconductor materials is an important topic since the performance (such as functionality and reliability) of electronic devices strongly depends on their mechanical properties [11–17].

Similar to most ceramics with a relatively limited tensile strain (less than 0.1%), bulk SiC is brittle at room temperature [18]. With the advancement of materials processing technology, micro- and nanoscale SiC components can be easily produced and they demonstrate promising

* Corresponding author.
E-mail address: xiaozhou.liao@sydney.edu.au (X. Liao).

http://dx.doi.org/10.1016/j.actamat.2014.07.055
1359-6454/

applications in micro- and nanoelectromechanical systems [19]. Available reports indicate that nanoscale SiC shows large plastic deformation through lattice breakage, lattice disorder and amorphization [20–22]. Phase transformation, which may also introduce plastic deformation, has been observed in SiC during annealing [23], thermal oxidation [24] and stressing at high temperature [25–27]. At room temperature, however, there is no experimental report on phase transformation in SiC crystals, although ab initio calculations suggest that a transformation occurs from tetrahedrally bonded SiC polytypes (e.g., ZB or WZ) to the rock salt (RS) structure at high pressure (>60 GPa) [28–30]. Since the occurrence of phase transformation may degrade the performance of SiC-related devices [8,31], the investigation of SiC polytypic phase transformation is practically important and, fundamentally, it can provide a better understanding of phase transformation in polytypic materials.

In this paper, we demonstrate solid evidence obtained from in situ deformation transmission electron microscopy (TEM) experiments that phase transformation can occur among single-crystal tetrahedrally bonded polytypic SiC nanopillars at room temperature. Additional insight into the phase transformation was obtained from molecular dynamics (MD) simulations. The reasons for the unexpected phase transformation in SiC nanopillars are discussed. Since polytypism is an interesting phenomenon in nature, this finding adds new insight to the physical understanding of the polytypic evolution in materials.

2. Experimental section

A commercial single crystal 4H–SiC (0 0 0 1) sample with a thickness of 300 μm was used in this study. The sample was cut into small rectangular pieces with lengths of 2 mm along a $\langle 1\,1\,\bar{2}\,0\rangle$ direction and widths of 1 mm parallel to a $\langle 1\,\bar{1}\,0\,0\rangle$ direction. Each piece was fixed to a 45° inclined platform on a tripod with the (0 0 0 1) plane faced to the platform and then mechanically ground until one edge of the sample was thinned to ~5 μm. The ground sample was taken off the platform and then pasted on a mount for pillar fabrication on the thin edge of the sample using a Zeiss Auriga focused ion beam scanning electron microscope. For coarse-milling, a 30 kV, 1 nA Ga^+ beam was used to fabricate the pillars into diameters of ~2 μm. The pillars were finally thinned to flat-top circular nanopillars with a diameter of ~180 nm using a 30 kV, 10 pA Ga^+ beam. Because of the use of a 45° platform, the (0 0 0 1) basal plane was ~45° off to the pillar surface (the surface normal is close to a $\langle 1\,\bar{1}\,0\,4\rangle$ direction), producing the large Schmid factor and therefore the corresponding resolved shear stress on the basal plane during deformation.

In situ deformation experiments of the pillars were conducted with a Hysitron PicoIndenter in a JEM-2100 TEM, with a flat diamond punch at a constant displacement rate of 10 nm s^{-1}. Raw load–displacement records were collected using the displacement-controlled mode of the PicoIndenter. The force and spatial resolutions are ~0.3 μN and 1 nm, respectively. Deformation processes of the nanopillars in TEM were recorded at 30 frames s^{-1} with a digital video recorder. From each recorded video and its corresponding load–displacement curve, it is possible to obtain an instantaneous force with its contact area between the diamond punch and nanopillar. To analyse the in situ mechanical testing data, stress is defined as the instantaneous force divided by the corresponding contact area between the punch and the nanopillar. To obtain reliable and repeatable data, eight nanopillars were tested.

MD simulations were performed to analyse the deformation process. A potential function consisting of pairwise and three-body covalent interactions was adopted to model the tetrahedral bonding in SiC [32]. To investigate the influence of diameter on the critical stress to initiate phase transformation, three samples were examined. All these samples have the same length of 32 nm with tip diameters of 5, 7 and 9 nm, and base diameters of 7, 9 and 11 nm, respectively. Atoms at the two ends of nanopillars with a thickness of 1.5 nm were frozen; these could play similar roles as the diamond punch and the base. The tapered angle is 2° according to the geometry of samples in the experiments. The [0 0 0 1] orientation of the 4H structure was inclined 45° with respect to the pillar axis. The motion of atoms was integrated using a Verlet leapfrog algorithm [33] with a time step of 2 fs. To obtain a free-standing configuration, each sample was relaxed for 20 ps before compression was applied. Compressive deformation was achieved in two steps. First, a modified isothermal–isobaric ensemble was used to reduce the pillar length with a strain rate of 2.5×10^{-3} ps^{-1} for 1 ps. In this step, a nominal strain of 0.25% was introduced at each deformation increment. The axial strain was then held and the pillar was relaxed for 6 ps through a canonical ensemble to calculate the mechanical properties of the pillar. The axial stress was calculated by the force acting on the frozen end, i.e., the tip with a diameter of 5, 7 and 9 nm, respectively, divided by the contact area. All calculations were performed with the DL_POLY2.20 package [34]. More details of the numerical simulations are provided in Ref. [22].

3. Results and discussion

Fig. 1a shows a linear load–displacement curve of a 4H–SiC pillar with a diameter of ~180 nm and a length of ~580 nm, respectively. The compressive deformation process stopped at a load of 275 μN (a stress of 9.0 GPa) without breaking the pillar. Fig. 1b and c presents the TEM images at the moment when the diamond punch just touched the pillar and at the deformation stage marked with the arrowhead in Fig. 1a, respectively. The TEM images were extracted from Movie 1 in the Supplementary materials. Three white arrows in Fig. 1c indicate bending contours in the pillar. These bending contours disappeared and the pillar returned to its original shape after being fully unloaded, as shown in Movie 1 in the Supplementary

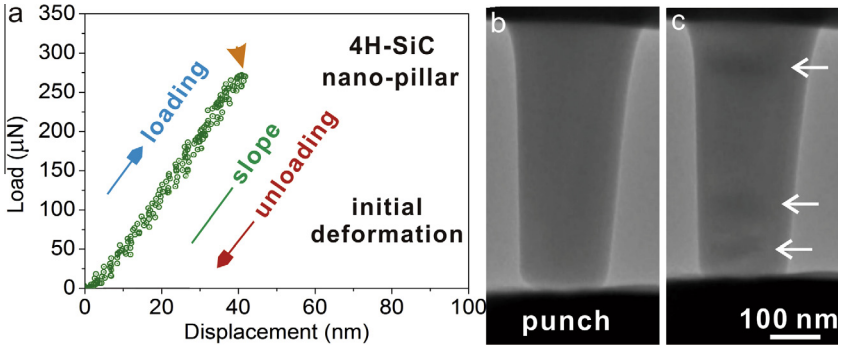

Fig. 1. (a) A load–displacement curve of a 4H–SiC pillar with a diameter of ~180 nm. (b, c) TEM micrographs extracted from Movie 1 in the Supplementary materials, corresponding to the initial state of the pillar (b) and final state (c) at the tip of the curve marked with an arrowhead in (a). Bending contours in (c) are marked with arrows.

materials, indicating the elastic nature of the deformation process.

Due to the slight tapering in the pillar, a model was derived to estimate the Young's modulus E of a tapered pillar based on the linear load–displacement record. It is assumed that there is no bending during small elastic deformations of the pillar. Fig. 2 shows a schematic diagram of a tapered pillar with the diameters at the lower and upper ends of d and D, respectively. Under a compressive load P, the displacement of the pillar is obtained by

$$U = \int_0^L \varepsilon(x)dx = \int_0^L \frac{P}{EA(x)}dx \tag{1}$$

where L is the pillar length and $\varepsilon(x)$ and $A(x)$ are the elastic strain and area of a cross-section at the position x, respectively. Based on the pillar geometry in Fig. 2, the area $A(x)$ is given by

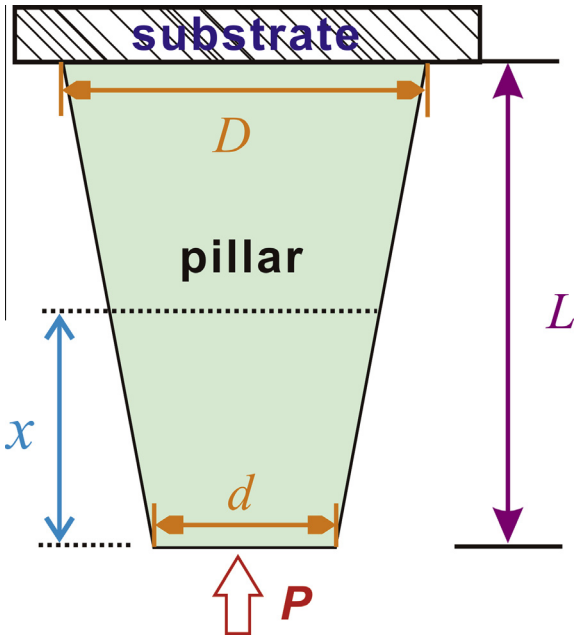

Fig. 2. A schematic diagram of a tapered pillar used for the derivation of Young's modulus. The diameters at the lower and upper ends of the pillar are d and D, respectively; L is the length of the pillar; and $A(x)$ corresponds to the cross-sectional area at the position.

$$A(x) = \frac{\pi}{4}\left(d + \frac{D-d}{L}x\right)^2 \tag{2}$$

Substituting Eq. (2) into Eq. (1), the Young's modulus of the tapered pillar becomes:

$$E = \frac{4}{\pi}\frac{L}{dD}K \tag{3}$$

where K ($=P/u$) is the stiffness, i.e., the slope from the load–displacement curve. Using Eq. (3) and the load–displacement data in Fig. 1a, the calculated Young's modulus of the 4H–SiC pillar oriented ~45° to the (0001) plane was ~135 GPa, which is smaller than that of [0001]-oriented 4H–SiC due to the anisotropy [35].

Fig. 3a shows the load–displacement behaviour of the pillar upon second loading to a higher load. There was a linear load–displacement relationship up to the stress level of 9.0 GPa (marked with a dotted arrow) with the slope 1 of the curve being the same as that in Fig. 1a. Beyond this point, a non-linear load–displacement relationship was observed with the load reaching 320 μN (a stress of 10.2 GPa). Interestingly, the unloading curve shows a different slope (slope 2) with respect to the loading curve. Estimation using Eq. (3) indicates that the Young's modulus is ~100 GPa for the slope 2, which is smaller than that for the slope 1. Fig. 3b (extracted from Movie 2 in the Supplementary materials) shows the deformation state at the peak stress marked with the arrowhead in Fig. 3a. Compared with the state at a stress level of 9.0 GPa (see Fig. 1c), more dark contrast areas identified by solid arrows were observed. After the pillar was fully unloaded, ~2% plastic strain remained in the pillar and some dark contrast lines/clusters persisted (see the dark contrast lines marked with solid arrows and dark contrast clusters marked with dotted arrows in Fig. 3c). The area enclosed by the load–displacement loop is the energy dissipated during the loading–unloading cycle and it can be measured with a digital planimeter. Dividing this by the volume of the nanopillar gives the energy per unit volume, which is ~290 MJ m^{-3}.

To understand the possible sources for the huge energy dissipation during mechanical deformation of the 4H–SiC

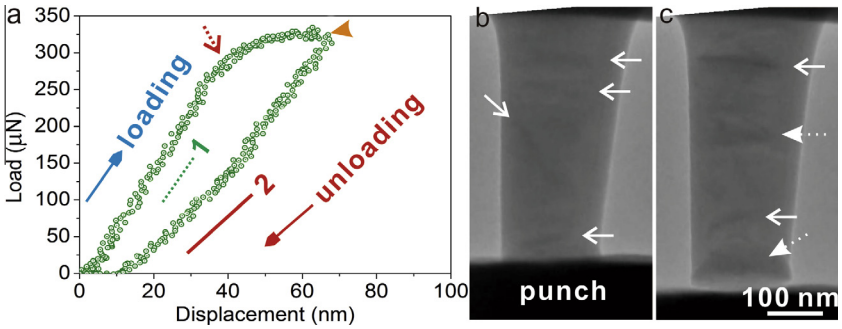

Fig. 3. (a) A load–displacement curve of the pillar beyond elastic deformation. The load increased linearly with displacement up to the position marked by a dotted arrow. The slope of the unloading curve (slope 2) is different from that of the loading curve (slope 1). (b, c) TEM images extracted from Movie 2 in the Supplementary materials, corresponding to the peak load (marked with an arrowhead in (a)) (b) and the final state after being fully unloaded (c). Dark contrast lines are marked with solid arrows while dark contrast clusters are indicated by dotted arrows.

nanopillars, detailed TEM characterization using selected area electron diffraction (SAED) and dark-field diffraction contrast imaging was conducted. Fig. 4a shows a diffraction pattern from a 4H–SiC matrix region without dark contrast in Fig. 3c. Although the diffraction pattern was not on a zone axis due to the single tilting nature of the TEM holder, a clear 4H–SiC related diffraction feature [36] was observed. At the dark cluster regions indicated by dotted arrows in Fig. 3c, a $\langle 1\,1\,0\rangle$ zone axis diffraction pattern from the cubic 3C SiC structure was obtained (Fig. 4b), indicating the occurrence of 4H → 3C phase transformation. A dark-field diffraction contrast image (Fig. 4c) obtained using a {0 0 2} diffraction spot shows two bright contrast areas marked with arrows, which correspond to the transformed 3C SiC phase areas embedded in the 4H matrix. Comparison of the stress levels shown in Figs. 1a and 3a indicates that the 4H → 3C phase transformation at room temperature occurs at a stress level exceeding 9.0 GPa. The phase transformation leads to the variation of the slopes (or corresponding Young's moduli) between the loading and unloading curves (3C is softer than 4H [35]), and the significant energy dissipation.

To identify the underlying mechanisms of the phase transformation, it is appropriate to recall the available reports on this issue. Table 1 lists the experimental and theoretical results of phase transformation in SiC under different conditions. Since the 3C polytype introduces a quantum well (QW) structure in the 4H structure [4,8,37], energy would be gained through electrons entering the QW-related states, which is energetically favourable for the 4H → 3C phase transformation during high-temperature annealing (>1000 °C) [23,38]. The 3C → 6H transformation occurs during annealing at ~2000 °C because the 3C polytype is stable at low temperature while 6H is the high temperature stable phase [39,40]. Oxidation-induced phase transformation is attributed to the lattice-mismatch-induced stress stemming from the doping difference between a SiC epilayer and its substrate [24]. Phase transformations during deformation at the temperature range of 400–1200 °C are due to the shear stress [25,27], thermodynamically favourable transition from a hexagonal structure to the stable 3C phase [26,27] and QW-related energy gain [26], respectively. In simulations, phase transformations from a ZB or WZ structure to a RS structure occur because most materials with low coordination number (CN) structures (for ZB and WZ, CN = 4) transform into a more compressed crystalline form with a higher CN (e.g. RS, CN = 6) at high pressure [28–30,41]. However, our experiments were conducted through deformation at room temperature, which is obviously different from those cases mentioned above.

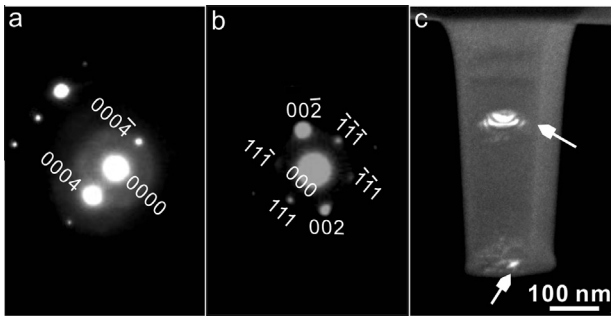

Fig. 4. SAED patterns obtained from a 4H–SiC matrix region (a) and a dark cluster region (b). (c) A dark-field TEM image of the pillar taken using a fcc {0 0 2} diffraction spot. The 3C regions (bright regions) are indicated using solid arrows.

The applied high stress should play a key role in the phase transformation of 4H–SiC nanopillars. In ceramic materials, a fracture process generally involves the initiation and subsequent propagation of cracks [42,43]. Crack initiation usually occurs at crystalline imperfections, which leads to stress concentration on the surface and in interior defects of materials. In bulk or thin film SiC crystals, dislocation motion and subsequent cracking limit the flow stress to only hundreds of MPa [27,44,45]. It is known that the number of pre-existing defects in a ceramic material diminishes with reducing material dimensions and that a defect-free crystal would be achieved when the dimensions are reduced to the nanoscale. This was the case for the nanoscale SiC single crystal examined in this study. The defect-free nature of the crystal significantly delayed the crack initiation in the SiC nanopillar, increased the strain and consequently the flow stress of the pillars. After the

Table 1
A summary of literature showing phase transformation and corresponding driving force in SiC.

Phase transformation	Conditions	Driving force	Refs.
4H → 3C	1150 °C annealing	QW action	[23,38]
4H → 3C	1150 °C oxidation	Lattice mismatch	[24]
4H → 3C	Compression at 400–700 °C	Phase stability + QW action	[26]
4H → 3C	Deformation (~120 MPa) at 900–1100 °C	Stress + thermodynamics	[27]
6H → 3C	Indentation (~50 MPa) at 1170 °C	Shear stress	[25]
3C → 6H	~2000 °C annealing	Phase stability	[39,40]
ZB → RS	>60 GPa (simulation)	High pressure	[28–30]
WZ → RS	600–700 GPa (simulation)	High pressure	[41]

flow stress exceeded 9.0 GPa as shown in Fig. 3, the phase transformation of 4H → 3C occurred.

MD simulations were performed to understand the experimental results. Fig. 5a shows the original state of a 4H–SiC nanopillar with a tip diameter of 5 nm. At the initiation stage of phase transformation, strain concentration occurs on the free surface of the sample, as shown in Fig. 5b, where atomic coordinates are extracted at a strain of 8.6% (point A in Fig. 5c) and the strain distribution is generated by means of the least squares atomic strain [46]. The 4H to 3C phase transformation is initiated at positions with strain concentration. Further analysis on the samples with a tip diameter of 7 and 9 nm demonstrates that such a behaviour is independent of diameters. The stress–strain curve of the 4H–SiC nanopillar with the tip diameter of 5 nm indicates that prior to a strain of 8.6%, the compressive deformation is purely elastic, with the stress reaching the maximum value of ~14.0 GPa. As the strain exceeds 8.6%, the stress quickly drops to 8.4 GPa due to the slip on the (0001) basal plane. Structural analysis reveals that, at a strain of 9.3%, a 3C grain is generated in the middle of the sample after the first slip (Fig. 5d).The phase transformation follows a stick–slip process with each stress drop corresponding to a slip event, where there is a stress range between which the phase transformation occurs. It indicates that the stress to initiate the first slip in the 4H–SiC nanopillar with a tip diameter of 5 nm is ~14.0 GPa while the stress of 8.4 GPa corresponds to the ending of the first slip. Fig. 5e shows the growth of the first 3C grain and the formation of the second 3C grain at the

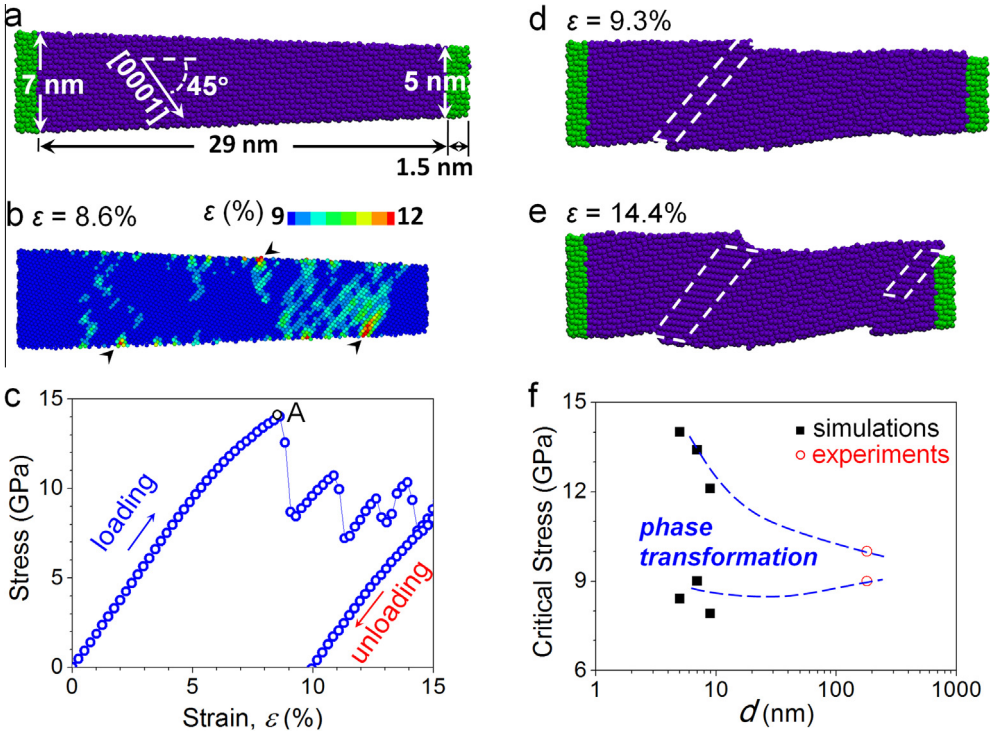

Fig. 5. (a) An image of a sample with a length of 32 nm and diameters of 5 and 7 nm at the tip and base, respectively. (b) The strain distribution at the initiation stage of phase transformation, where arrowheads denote positions of strain concentration. (c) A typical stress–strain curve obtained from MD simulations. (d) A 3C grain forms in the middle of the sample after the first slip. (e) A snapshot image of the nanopillar at a strain of 14.4%. Areas in which the 3C phases formed are marked by two dashed parallelograms. (f) The critical stress to initiate phase transformation decreases as the diameter of 4H–SiC nanopillars increases. Dashed curves show the expected trends.

tip of the sample after multiple slips. The locations of the two 3C grains are indicated using two dashed parallelograms in Fig. 5e. The locally formed 3C grains in the 4H matrix remain after the external load is removed. The phase transformation sites are consistent with in situ experimental observation. It is seen from Fig. 5c that the unloading curve has a slightly lower slope than that of the loading one, which is less obvious than that displayed in the experimental data. This is because the atomic interactions for 4H– and 3C–SiC structures are indistinguishable in the potential function [32] used in the modelling. Moreover, as the tip diameter increases to 9 nm, the critical stress to initiate phase transformation reduces to 7.9–12.1 GPa (Fig. 5f). Note that the stress values obtained from MD simulations are higher than but still in relatively good agreement with the experimental ones (see Fig. 5f). The difference between experiments and simulations are due to three possible reasons: (i) the strain rate in MD simulations is generally in the order of $10^8\ s^{-1}$ [47–49], which is significantly larger than that in experiments ($\sim 10^{-2}\ s^{-1}$); (ii) since calculations for large objects are extremely time-consuming, only small sample dimensions with diameters of 5–9 and 7–11 nm at the contact and base sites, respectively, were used in the MD simulations, which are much smaller than the sample diameters of 180–220 nm in the experiments; and (iii) the electron-beam irradiation during the deformation experiments may lower the energy barrier for the phase transformation through providing extra energy to the samples.

The MD simulations also indicate that the 4H to 3C phase transformation originates from the slip between the neighbouring close-packed planes. In the tetrahedral bonding cases of SiC structures, there are three basic close-packed sites denoted as A, B and C, see Fig. 6a. The 4H structure adopts the periodic ABCB stacking sequence. Each ABC stacking unit in a 4H cell can be regarded as a 3C inclusion; see the shadowed area in column "Step 0" in Fig. 6b. Thus, a boundary divides the 4H structure and the 3C inclusion into two parts. Slip of the 4H region along the boundary with a Burgers vector of $1/3\langle 1\bar{1}00\rangle$ changes the stacking sequence in the 4H region, i.e., A → C, B → A and C → B, respectively. Fig. 6b shows three original 4H units, containing 12 layers. The boundary lies between the third and fourth layers. The first slip (Step 1 in Fig. 6b) moves the fourth B layer to site A, leading to the growth of the original 3C seed from ABC to ABCA. Thus, the boundary ascends one layer up to between the fourth and fifth layers. At Step 2, ongoing slip shifts the fifth, sixth and seventh layers to sites B, C and A. Then, the 3C grain grows to ABCABCA, with the boundary ascending the layers up to between the seventh and eighth layers. The 3C grain continuously grows by repeating Steps 1 and 2, resulting in the growth of the 3C region in the 4H matrix.

It is worth noting that the effect of electron-beam irradiation on the phase transformation cannot be ruled out since the deformation experiments were conducted in TEM. However, the electron-beam irradiation effect should not be a major driving force because: (i) one of the pillars was tested in the TEM under irradiation (without mechanical stress) for more than 2 h and no phase transformation was observed; (ii) the irradiation-induced temperature rise should be small since the electron beam intensity was very weak ($\sim 10^{-3}\ A\ cm^{-2}$); and (iii) MD simulations indicated that the 4H → 3C phase transformation occurs without any electron-beam irradiation.

To understand the deformation behaviour after the phase transformation, the pillar was further compressed until fracture. Fig. 7 shows its load–displacement curve and corresponding TEM images. The TEM images were extracted from Movie 3 in the Supplementary materials. The slope of the loading curve (indicated by a solid line) is the same as that of slope 2 after the occurrence of the 4H → 3C phase transformation in Fig. 3a, indicating that the phase transformation is permanent. Fig. 7b shows a TEM image of the pillar at the deformation stage just

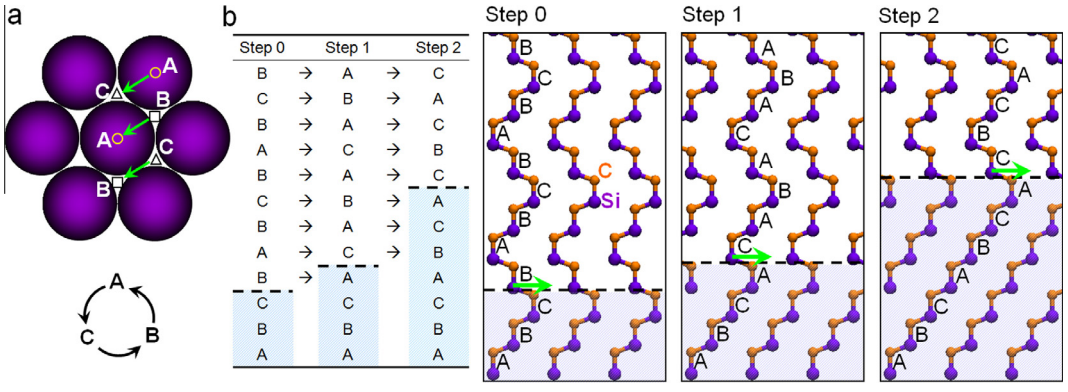

Fig. 6. (a) Three tetrahedral A, B and C stacking sites are represented by circles (○), boxes (□) and triangles (Δ), respectively, on a close-packed crystalline plane. Slip along a direction on the (0001) plane with a Burgers vector of $1/3\ \langle 1\bar{1}00\rangle$ moves atoms at A, B and C sites to C, A and B sites, respectively. The slip sketch is also depicted at the lower panel. (b) Each ABC stacking unit in a 4H structure consists of a 3C seed (the shaded region). The 3C grain grows via repeated slips between 4H and 3C structures along their boundaries (dashed lines). Green arrows represent the slip direction. (For interpretation of the references to color in this figure legend, the reader is referred to the web version of this article.)

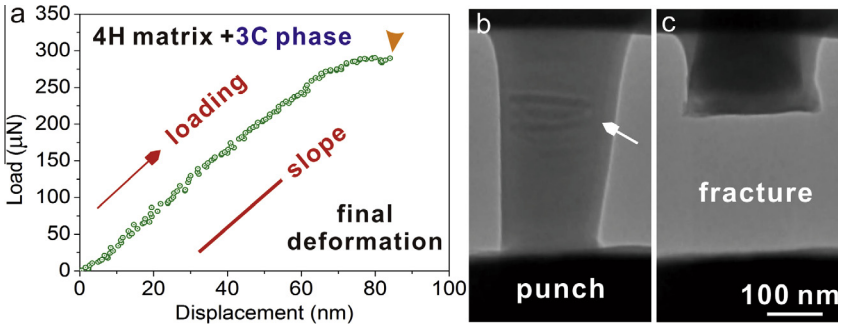

Fig. 7. (a) The load–displacement curve of the 4H–SiC pillar for the final fracture testing. (b, c) TEM images extracted from Movie 3 in the Supplementary materials, which correspond to the states of the pillar just before (marked with the arrowhead in (a)) and after fracture.

before fracture (the top 3C inclusion is marked with an arrow), which corresponds to the tip marked with an arrowhead in the load–displacement curve in Fig. 7a. Fracture occurred at a place near the top 3C phase region (Fig. 7c). The total strain of the SiC nanopillar at fracture was estimated to be ~15%. The large deformability is attributed to the size effect that crack initiation is significantly delayed because of the absence of flaws inside the nanoscale pillars.

4. Conclusions

Room-temperature in situ deformation TEM investigation shows that 4H–SiC nanopillars can be elastically compressed up to a stress level of 9.0 GPa. Further deformation leads to the 4H → 3C phase transformation, resulting in the change of the Young's modulus of the nanopillars. Based on the MD simulations, the phase transformation initiates at a stress of 12.1–14.0 GPa; however, the stress quickly drops to 7.9–9.0 GPa after the slip, which is close to the experimentally measured transformation stress of 9–10 GPa. The phase transformation due to the slip on the (0001) plane along a $\langle 1\bar{1}00\rangle$ direction and the corresponding atomistic layer transformation from 4H to 3C have been simulated. The observed phase transformation is attributed to the high flow stress accessible in nanoscale pillars.

Acknowledgements

We are grateful for the scientific and technical input and support from the Australian Microscopy and Microanalysis Research Facility node at the University of Sydney: Sydney Microscopy & Microanalysis. This research has been supported by the Australian Research Council (DP0985450 and FT110100236), the National Natural Science Foundation of China (Grant Nos. 11172024, 11232013 and 11372022), the National Basic Research Program of China (2012CB937500), the Opening Fund of State Key Laboratory of Nonlinear Mechanics and the Research Grant Council of the Hong Kong Special Administrative Region, China (Project No. City U 120611 (9041679)). MD simulations were conducted at iVEC through the use of advanced computing resources located at iVEC@Murdoch. Partial computational resources were provided by the Intersect Australia Ltd.

Appendix A. Supplementary data

Movies 1–3, from which the snapshot images were extracted and presented in Figs. 1, 3 and 7, respectively, are provided. Supplementary data associated with this article can be found, in the online version, at http://dx.doi.org/10.1016/j.actamat.2014.07.055.

References

[1] Jepps NW, Page TF. Prog Cryst Growth Charact 1983;7:259.
[2] Chen B, Gao Q, Chang L, Wang YB, Chen ZB, Liao XZ, et al. Acta Mater 2013;61:7166.
[3] Chen B, Matsuhata H, Sekiguchi T, Ohyanagi T, Kinoshita A, Okumura H. Appl Phys Lett 2010;96:212110.
[4] Chen B, Sekiguchi T, Ohyanagi T, Matsuhata H, Kinoshita A, Okumura H. Phys Rev B 2010;81:233203.
[5] Fissel A. Phys Rep 2003;379:149.
[6] Ha S, Skowronski M, Sumakeris JJ, Paisley MJ, Das MK. Phys Rev Lett 2004;92:175504.
[7] Galeckas A, Linnros J, Pirouz P. Phys Rev Lett 2006;96:025502.
[8] Skowronski M, Ha S. J Appl Phys 2006;99:01110.
[9] Fabbri F, Rossi F, Melucci M, Manet I, Attolini G, Favaretto L, et al. Nanoscale Res Lett 2012;7:680.
[10] Chen B, Matsuhata H, Kumagai K, Sekiguchi T, Ichinoseki K, Okumura H. J Appl Phys 2012;111:053513.
[11] Chen J, Chen B, Sekiguchi T, Fukuzawa M, Yamada M. Appl Phys Lett 2008;93:112105.
[12] Yang RS, Qin Y, Dai LM, Wang ZL. Nat Nanotechnol 2009;4:34.
[13] Cao J, Ertekin E, Srinivasan V, Fan W, Huang S, Zheng H, et al. Nat Nanotechnol 2009;4:732.
[14] Pillarisetty R. Nature 2011;479:324.
[15] Chen B, Gao Q, Wang YB, Liao XZ, Mai YW, Tan HH, et al. Nano Lett 2013;13:3169.
[16] Chen B, Wang J, Gao Q, Chen YJ, Liao XZ, Lu CS, et al. Nano Lett 2013;13:4369.
[17] Kim YJ, Lee WW, Choi IC, Yoo BG, Han SM, Park HG, et al. Acta Mater 2013;61:7180.
[18] Pirouz P, Demenet JL, Hong MH. Philos Mag A 2001;81:1207.
[19] Feng XL, Matheny MH, Zorman CA, Mehregany M, Roukes ML. Nano Lett 2010;10:2891.

[20] Han XD, Zhang YF, Zheng K, Zhang XN, Zhang Z, Hao YJ, et al. Nano Lett 2007;7:452.
[21] Zhang YF, Han XD, Zheng K, Zhang Z, Zhang XN, Fu JY, et al. Adv Funct Mater 2007;17:3435.
[22] Wang J, Lu C, Wang Q, Xiao P, Ke FJ, Bai YL, et al. Nanotechnology 2012;23:025703.
[23] Chung HJ, Liu JQ, Skowronski M. Appl Phys Lett 2002;81:3759.
[24] Okojie RS, Xhang M, Pirouz P, Tumakha S, Jessen G, Brillson LJ. Appl Phys Lett 2001;79:3056.
[25] Yang JW, Pirouz P. J Mater Res 1993;8:2902.
[26] Idrissi H, Lancin M, Douin J, Regula G, Pichaud B. Mater Sci Forum 2005;483–485:299.
[27] Lara A, Castillo-Rodriguez M, Munoz A, Dominguez-Rodriguez A. J Eur Ceram Soc 2012;32:495.
[28] Yoshida M, Onodera A, Ueno M, Takemura K, Shimomura O. Phys Rev B 1993;48:10587.
[29] Miao MS, Lambrecht WRL. Phys Rev B 2003;68:092103.
[30] Sarasamak K, Kulkarni AJ, Zhou M, Limpijumnong S. Phys Rev B 2008;77:024104.
[31] Bergman JP, Lendenmann H, Nilsson PÅ, Lindefeldt U, Skytt P. Mater Sci Forum 2001;353–356:299.
[32] Vashishta P, Kalia RK, Nakano A, Rino JP. J Appl Phys 2007;101:103515.
[33] Allen MP, Tildesley DJ. Computer simulation of liquids. Oxford: Clarendon Press; 1989.
[34] Smith W, Yong CW, Rodger PM. Mol Simul 2002;28:385.
[35] Konstantinova E, Bell MJV, Anjos V. Intermetallics 2008;16:1040.
[36] Chen B, Matsuhata H, Sekiguchi T, Ichinoseki K, Okumura H. Acta Mater 2012;60:51.
[37] Chen B, Matsuhata H, Sekiguchi T, Kinoshita A, Ichinoseki K, Okumura H. Appl Phys Lett 2012;100:132108.
[38] Liu JQ, Chung HJ, Kuhr T, Li Q, Skowronski M. Appl Phys Lett 2002;80:2111.
[39] Jepps NW, Page TF. In: Krishna P, editor. Progress in crystal growth and characterization, vol. 7. New York: Pergamon Press; 1983. p. 256–306.
[40] Vlaskina SI, Mishinova GN, Vlaskin VI, Rodionov VE, Svechnikov GS. Semicond Phys Quantum Electron Optoelectron 2011;14:432.
[41] Durandurdu M. Phys Rev B 2007;75:235204.
[42] Wang YB, Wang LF, Joyce HJ, Gao Q, Liao XZ, Mai YW, et al. Adv Mater 2011;23:1356.
[43] Jang DC, Meza LR, Greer F, Greer JR. Nat Mater 2013;12:893.
[44] Lu CS, Danzer R, Fischer FD. Phys Rev E 2002;65:067102.
[45] Lu CS, Danzer R, Fischer FD. J Eur Ceram Soc 2004;24:3643.
[46] Shimizu F, Ogata S, Li J. Mater Trans 2007;48:2923.
[47] Ngan AHW, Zuo L, Wo PC. Proc R Soc A 2006;462:1661.
[48] Li XY, Wei YJ, Lu L, Lu K, Gao H. Nature 2010;464:877.
[49] You ZS, Li XY, Gui LJ, Lu QH, Zhu T, Gao H, et al. Acta Mater 2013;61:217.